Supporting Information

Efficient Bifunctional Water Splitting Catalysts Enabled by Crystalline-Amorphous Ni_xS_y@NiFe LDH Heterojunctions

Shaobo Ye, Yong Xu, Xiaoyu Bai, Zhao Liang, Qiao Liu, Qiliang Wei, Dongjiang Yang, Weiyou Yang, Fengmei Gao and Qing Shi**

Institute of Micro/Nano Materials and Devices, Ningbo University of Technology, Ningbo City, 315211, P. R. China.

1. Experimental Section

1.1. Chemicals and materials

Ethanediamine (AR), powdered sulfur (AR), ethanol (99.7%), and potassium hydroxide (KOH, 90%) were utilized in this study. The Pt/C (20%) catalyst was procured from Tanaka Kikinzoku Kogyo K.K., while the RuO_2 was purchased from Aladdin Reagent (Shanghai) Co., Ltd. All chemical reagents were employed as received without further purification. Deionized (DI) water with an impedance value of 18.2 Ω was sourced using an ultrapure water purification system.

1.2. Synthesis of Ni_xS_y

Nickel sulfide (Ni_xS_y) supported on nickel foam (NF) was synthesized via a hydrothermal method. Specifically, a 2 × 3 cm² piece of NF was first immersed in 2 M HCl for 15 min to remove the surface oxide layer, followed by thorough washing with ethanol and deionized water, and subsequent drying under vacuum environment. For the hydrothermal synthesis, 60 mg of sulfur powder, 16 mL of 99.7% ethanol, and 16 mL of ethylenediamine were mixed and transferred into a 50 mL Teflon-lined stainless steel autoclave. A pre-cleaned piece of NF was immersed in the solution, and the autoclave was sealed and heated to 160 °C for 6 h. After the reaction, the resulting Ni_xS_y/NF was washed with ethanol and dried under vacuum at room temperature. To investigate the effect of S content, the amount of S powder was varied to 20, 30, 40, 50, and 70 mg, yielding Ni_xS_y/NF-20, Ni_xS_y/NF-30, Ni_xS_y/NF-40, Ni_xS_y/NF-50, and Ni_xS_y/NF-70 samples, respectively.

1.3. Synthesis of Ni_xS_y@NiFe LDH

Ni_xS_y@NiFe LDH was prepared using a chemical soaking method. Typically, a 1 × 3 cm² piece of Ni_xS_y/NF was immersed in 16 mL of an aqueous $FeCl_3 \cdot 6H_2O$ solution (0.04 mol/L) and allowed to stand at room temperature for 30 min. After the reaction, the sample was thoroughly rinsed with deionized water and ethanol, yielding Ni_xS_y@NiFe LDH-30. To explore the effect of the soaking time, which was varied to 10, 20, 40, and 50 min, resulting in the synthesis of Ni_xS_y@NiFe LDH-10, Ni_xS_y@NiFe LDH-20, Ni_xS_y@NiFe LDH-40, and Ni_xS_y@NiFe LDH-50 samples, respectively.

1.4. Materials characterization

The phase composition of the materials was analyzed using a focused X-ray diffractometer (XRD, RINT2000 V/PC, Bruker). Scanning electron microscopy (SEM) images were obtained on a Hitachi S-4800 at an acceleration voltage of 10 kV. Transmission electron microscopy (TEM) and high-resolution TEM (HRTEM)

images were acquired using a Tecnai G F20. Additionally, the elemental composition and surface chemical states were analyzed by X-ray photoelectron spectroscopy (XPS, Scientific KAlpha, Thermo, USA), with the C 1s peak at 284.8 eV used as an internal reference. Raman spectroscopy (Renishaw inVia-Reflex) with a 532 nm laser was employed for microstructural analysis and in situ Raman testing.The metal element content wasevaluated by inductively coupled plasma atomic emission spectroscopy (ICP−OES, Agilent, USA).

1.5. Electrochemical tests

All electrochemical tests were carried out in a 1 M potassium hydroxide solution that had been purged with nitrogen (N_2), where the prepared electrode served as the working electrode, a graphite rod was used as the counter electrode, and Hg/HgO (1 M KOH) acted as the reference electrode. All measured potentials were converted to the reversible hydrogen electrode (RHE) using the formula: $E_{RHE} = E_{(Hg/HgO)} + 0.9253$ for 1 M KOH. Cyclic voltammograms curves (CV) were first measured by using an electrochemical workstation (Corr Test, CS2350H) at a scan rate of 10 mV/s to activate the electrodes. Subsequently, linear sweep voltammograms (LSV) curves were recorded at a slow scan rate of 1 mV/s. The Tafel slope was determined by fitting the linear region of the LSV curve according to the equation $\eta = b \log(j) + a$, where j is the current density and b is the Tafel slope. Electrochemical impedance spectroscopy (EIS) was carried out over a frequency range of 10^6 Hz to 0.1 Hz with testing potentials of -0.12 V vs. RHE for the hydrogen evolution reaction (HER) and 1.58 V vs. RHE for the oxygen evolution reaction (OER).

The electrochemical active surface area (ECSA) was estimated from the double-layer capacitance (C_{dl}), which was calculated from CV measurements performed at scan rates ranging from 20 to 100 mV/s. Specifically, C_{dl} was calculated from the slope of the $\Delta j/2$ versus scan rate relationship, where $\Delta j = j_a - j_c$ (j_a and j_c are the anodic and cathodic current densities at the medium potential, respectively). ECSA was then calculated as $ECSA = C_{dl}/C_s$, where C_s is the specific capacitance of a smooth electrode, taken as 0.04 mF cm^{-2}. Additionally, stability tests for HER and OER were conducted for 250 h at a constant current density of -200 mA cm^{-2} and 200 mA cm^{-2}, respectively.

Linear sweep voltammetry (LSV) was employed to measure the reduction peak currents at various scan rates. A linear regression plot of the reduction peak current versus scan rate was constructed to determine the slope through curve fitting. The m can be obtained by the following equation:

$$\text{slope} = \frac{n^2F^2m}{4RT}$$

where n is the number of electron transfer, which is taken as 1; R is the ideal gas constant (8.314 $J \cdot K^{-1} \cdot mol^{-1}$), and T is the absolute temperature (298 K).The conversion frequency (TOF) was calculated using the formula:

$$\text{TOF} = \frac{A \times J}{4Fm}$$

where J represents the current density, A is the electrode area, 4 is the number of electrons transferred to generate 1 mole of O_2, F is Faradaic constant (96485 C mol^{-1}), and m represents the number of active sites.

The roughness factor (R_f) of the electrode materials was estimated by the following equation previously reported in the literature[1].

$$R_f = \frac{ECSA\ (cm^2)}{geometrical\ surface\ area\ of\ eletrode(cm^2)}$$

where, ECSA- electrochemically active surface area (cm^2)

1.6 Computational Method

Computational Models for HER

All calculations were performed using the Vienna Ab initio Simulation Package (VASP), employing Density Functional Theory (DFT) as the computational framework. The exchange-correlation interactions were described using the Generalized Gradient Approximation (GGA) with the Perdew-Burke-Ernzerhof (PBE) functional. As to HER, the (110) crystallographic plane of Ni_3S_2 and the (100) plane of NiFe LDH were selected as interfacial contact surfaces, with a sulfur-oxygen co-existing buffer layer introduced at the interface transition region to ensure electronic structure continuity. To satisfy lattice matching requirements, a 3×1 supercell of Ni_3S_2 (110) plane and a 2×1 supercell of NiFe LDH (100) plane were periodically extended, achieving minimized lattice mismatch through averaged lattice parameter method. Within the plane-wave ultrasoft pseudopotential framework, all computational models incorporated a vacuum layer ≥15 Å along the non-periodic direction to eliminate mirror-image interactions. During geometry optimization, positional constraints (fixed Cartesian coordinates) were applied to the lowest Ni and S layer, while allowing full-degree relaxation for the rest of sites.

Computational Models for OER

The DFT calculations for the oxygen evolution reaction (OER) were performed on two structural models: pristine NiOOH and the NiOOH@NiFeOOH heterostructure. For the pristine NiOOH model, the (001) facet of β-NiOOH was selected due to its demonstrated catalytic effectiveness in alkaline OER conditions. The NiOOH@NiFeOOH heterostructure model was constructed by coupling the (001) facets of β-NiOOH and NiFeOOH phases, as this interface has been reported to significantly enhance OER activity. The supercell configuration was built by periodically extending a 2×3 supercell of β-NiOOH (001) and matching it with a compatible NiFeOOH (001) supercell to minimize lattice mismatch. All slab models included a vacuum gap of at least 15 Å along the z-direction to eliminate interactions between periodic slab images. Geometry optimization was carried out with convergence criteria of 1.0×10^{-5} eV for total energy and 0.02 eV/Å for atomic forces.

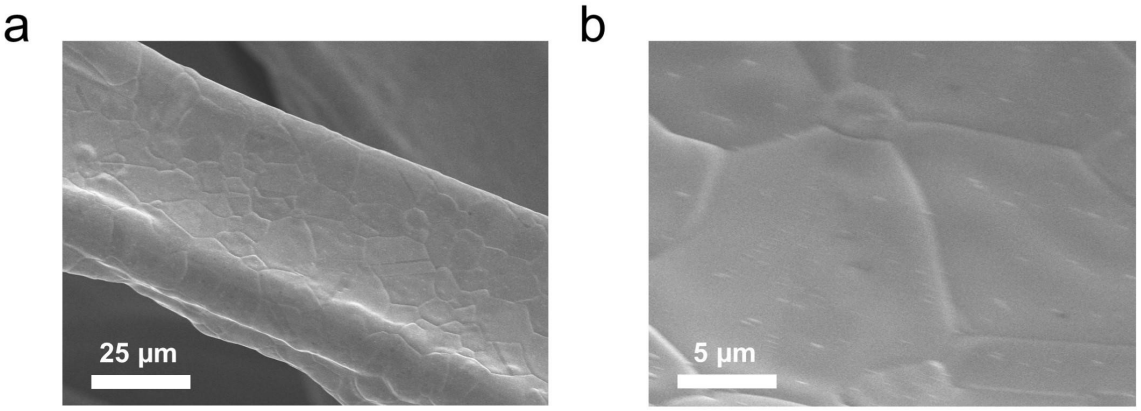

Figure S1. SEM images of Ni foam at low and high magnifications.

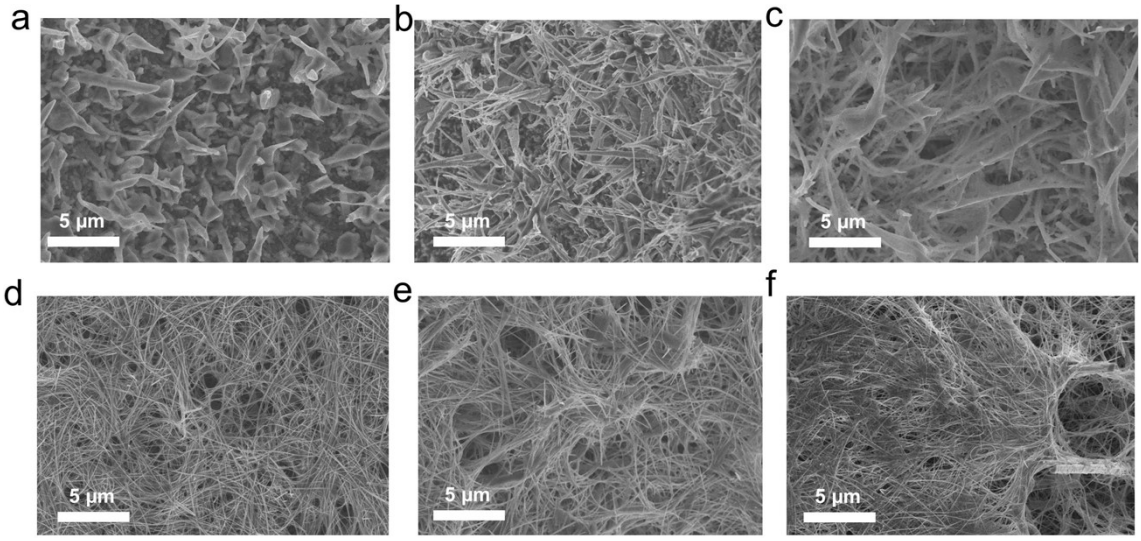

Figure S2. SEM images of different S powder addition amounts: (a) 20 mg; (b) 30 mg; (c) 40 mg; (d) 50 mg; (e) 60 mg; and (f) 70 mg.

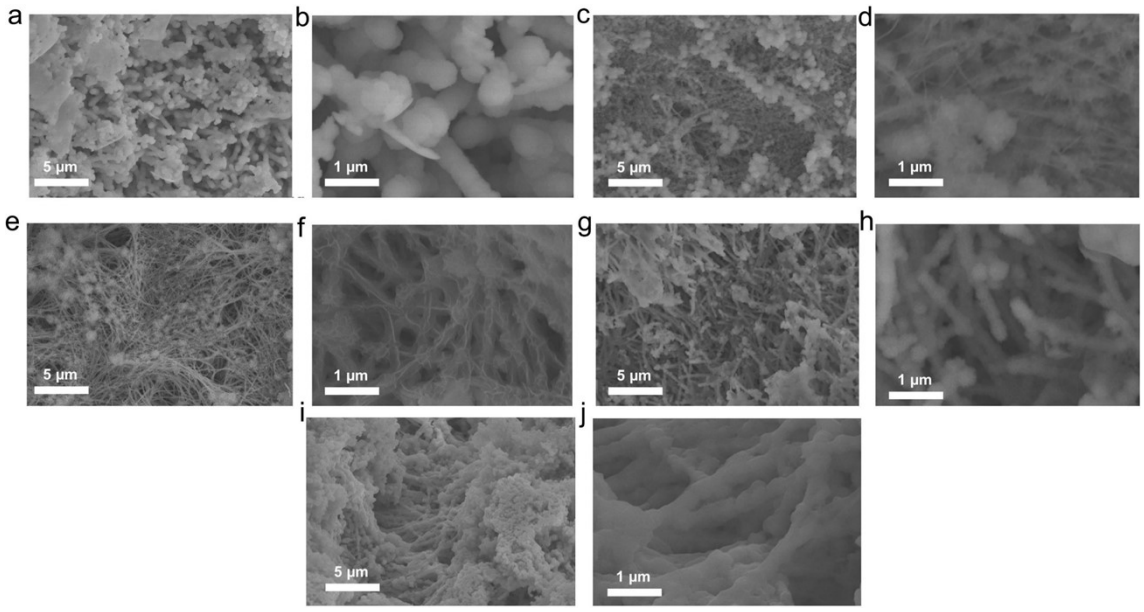

Figure S3. SEM images of Ni_xS_y@NiFe LDH at different soaking times : (a-b) 10 min; (c-d) 20 min; (e-f) 30 min; (g-h) 40 min; (i-g) 50 min.

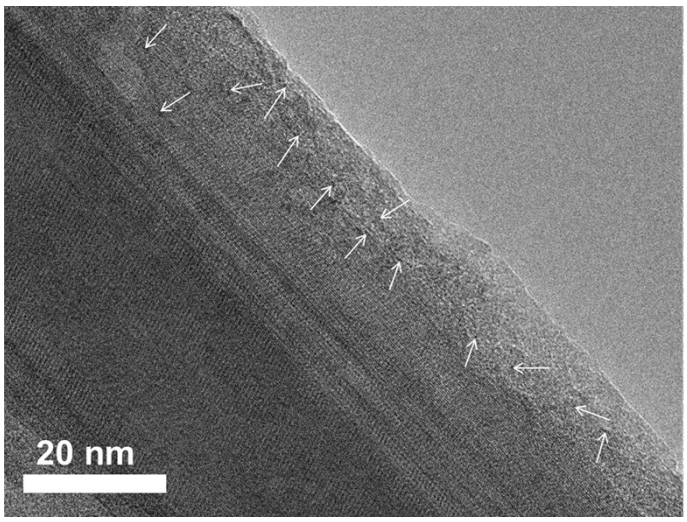

Figure S4. HRTEM images of Ni_xS_y@NiFe LDH.

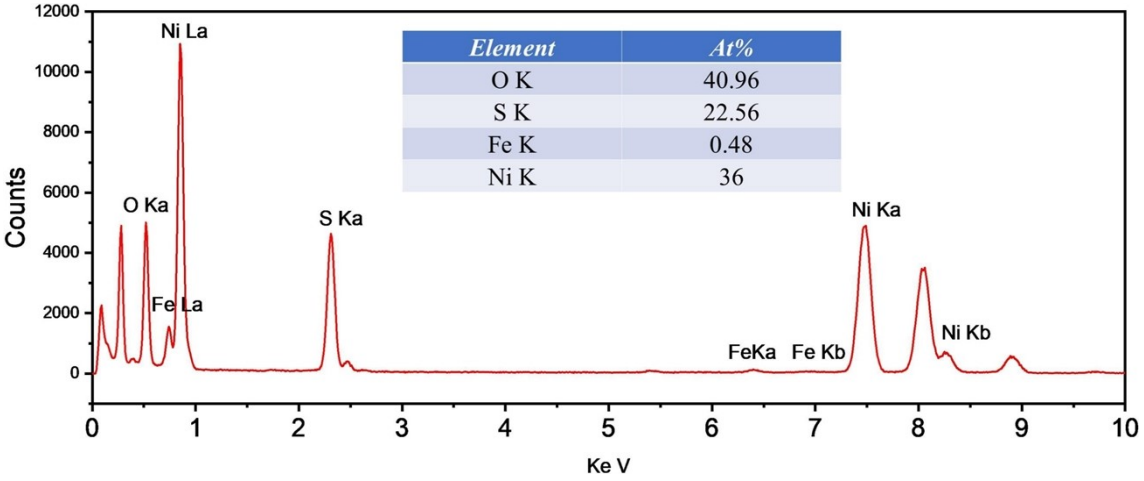

Figure S5. EDS spectra of Ni_xS_y@NiFe LDH.

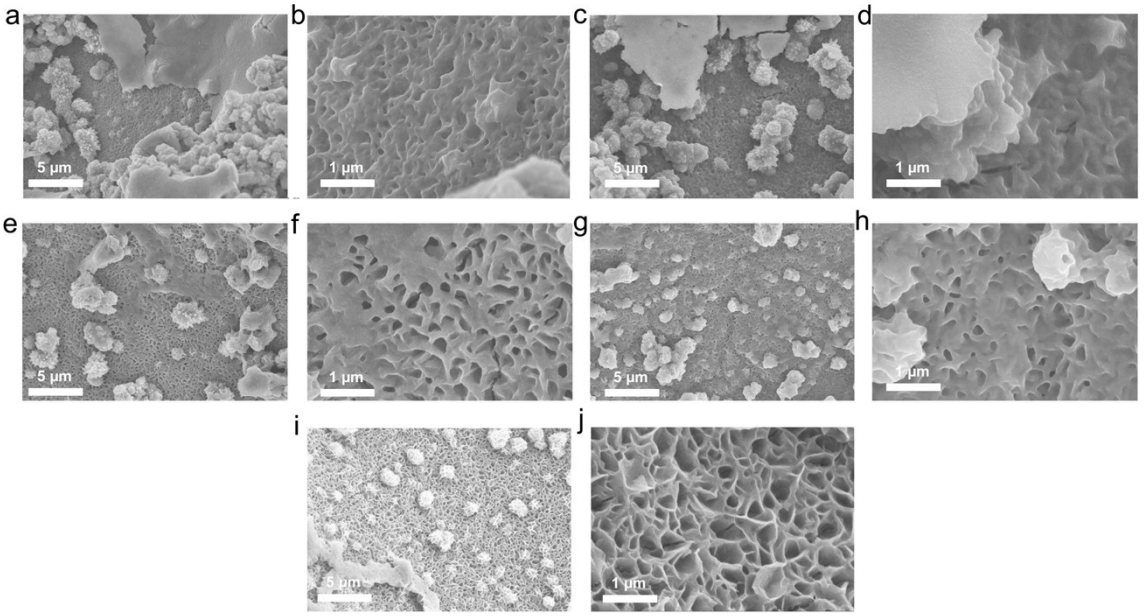

Figure S6. SEM images of Ni foam etched by $FeCl_3 \cdot 6H_2O$ at different times :(a-b) 10 min; (c-d) 20 min; (e-f) 30 min; (g-h) 40 min; (i-j) 50 min.

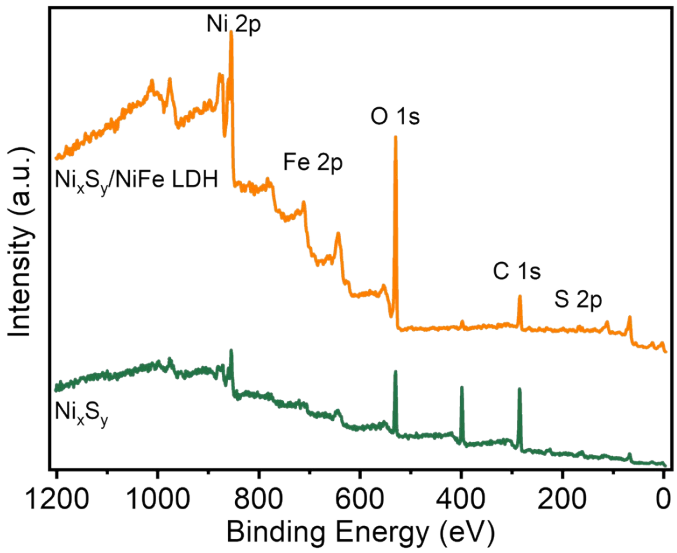

Figure S7. XPS survey of Ni_xS_y and Ni_xS_y@NiFe LDH.

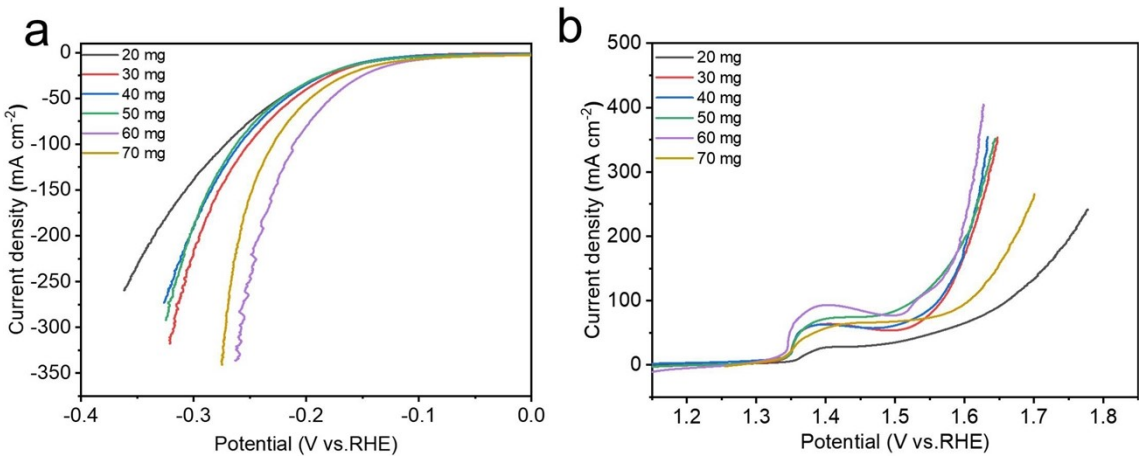

Figure S8. The Ni_xS_y polarization curves were obtained for various quantities of S powder. It is noteworthy that the electrode exhibits superior HER and OER activity when the dosage of S powder reaches 60 mg.

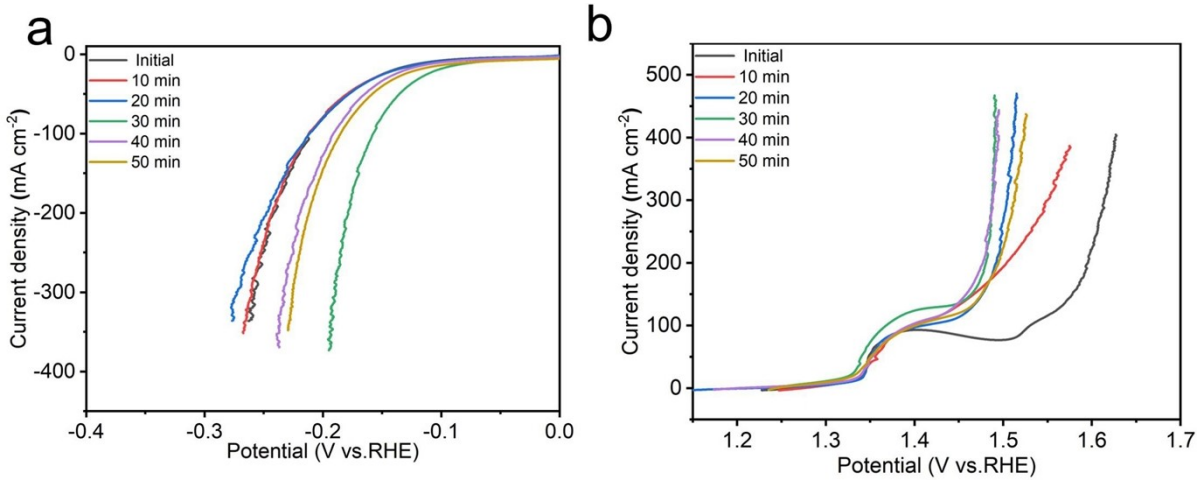

Figure S9. The Ni_xS_y@NiFe LDH polarization curves were examined under various soaking conditions of $FeCl_3$ solution. Remarkably, the electrode exhibited superior HER and OER activity when subjected to a 30-minute soaking time.

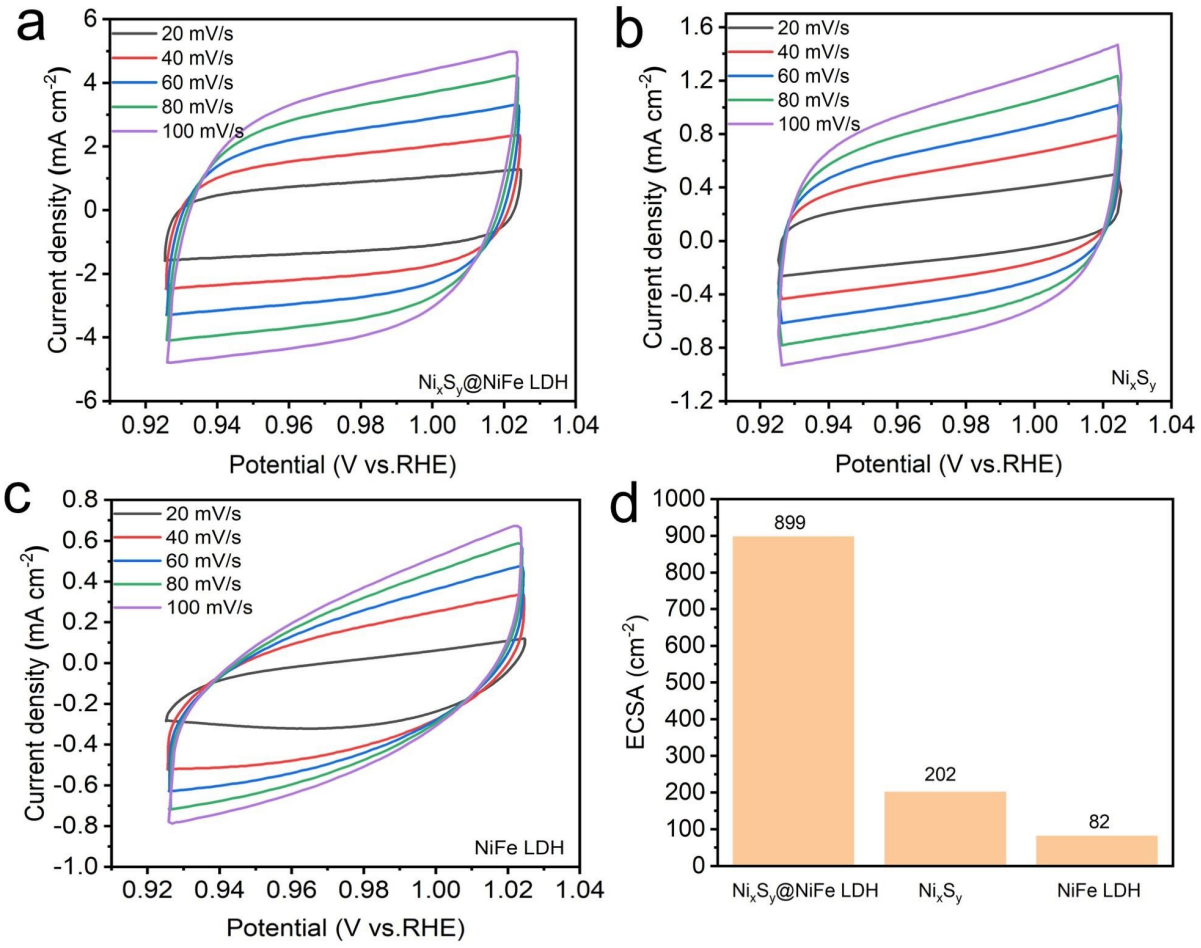

Figure S10. Cyclic voltammetry curves of (a) Ni_xS_y@NiFe LDH, (b) Ni_xS_y, (c) NiFe LDH in the region of 0.93-1.03 V vs. RHE. (d) The ECSA values of the fabricated samples.

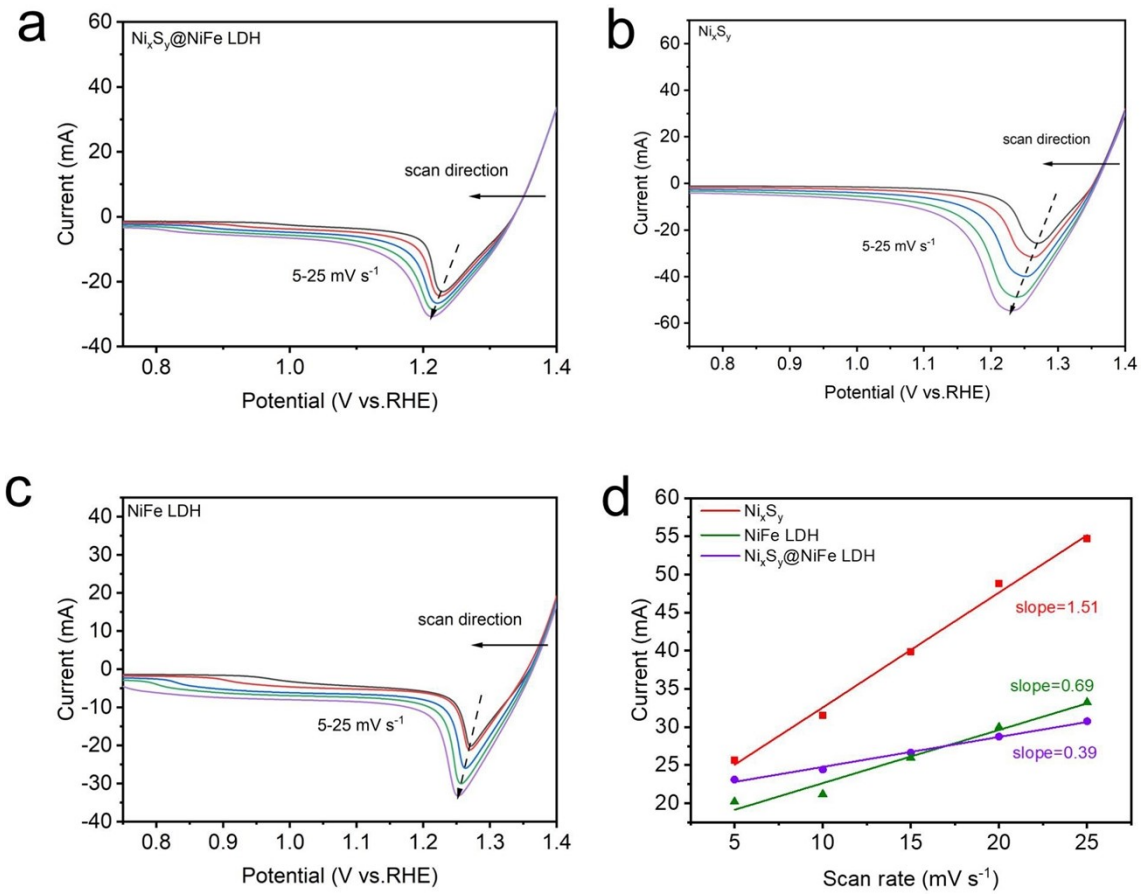

Figure S11. CV curves of (a) Ni_xS_y@NiFe LDH, (b) Ni_xS_y and (c) NiFe LDH at different scan rates; (c) current density of the peak prior to OER current versus scan rates.

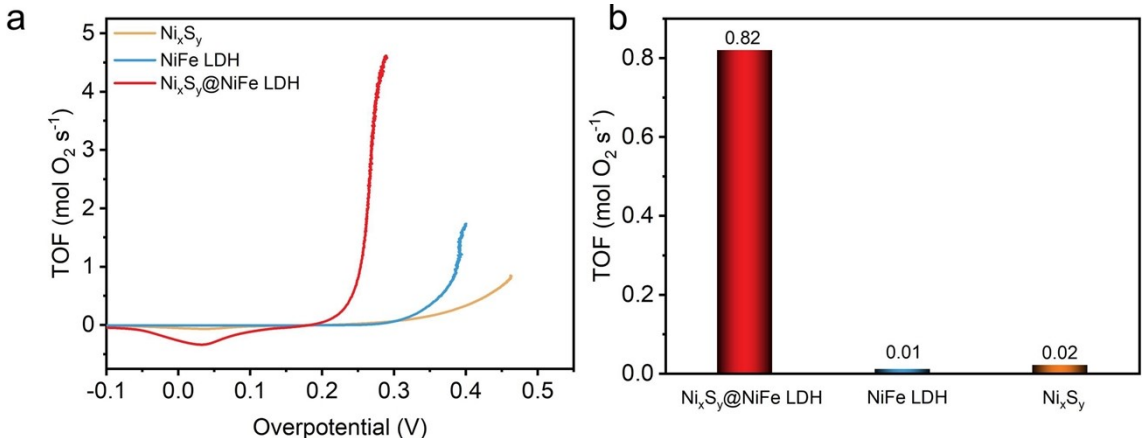

Figure S12. (a) Plot of the TOF of Ni_xS_y@NiFe LDH, Ni_xS_y and NiFe LDH as a function of the overpotential. (b) TOF values of the as-prepared catalysts for OER at an overpotential of 250 mV.

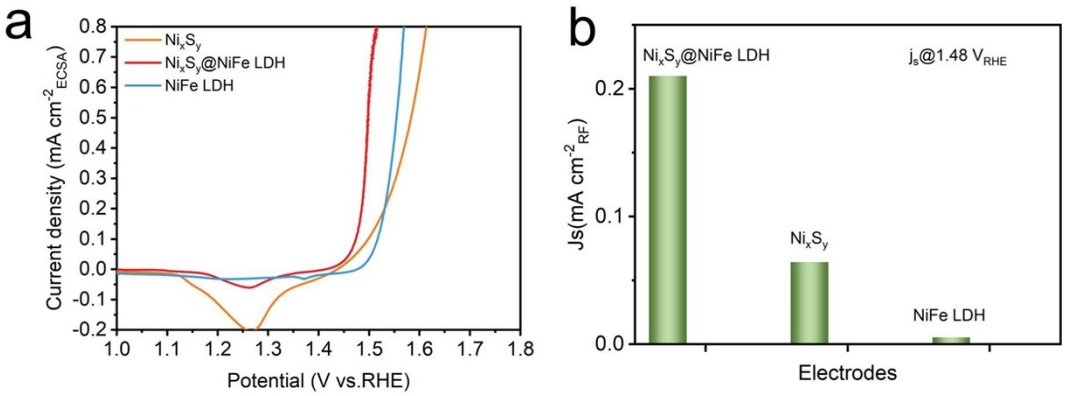

Figure S13. (a) ECSA normalized OER current densities (j_{ECSA}) of the electrodes. (b) The specific activity of the as-prepared electrodes at 1.48 VRHE.

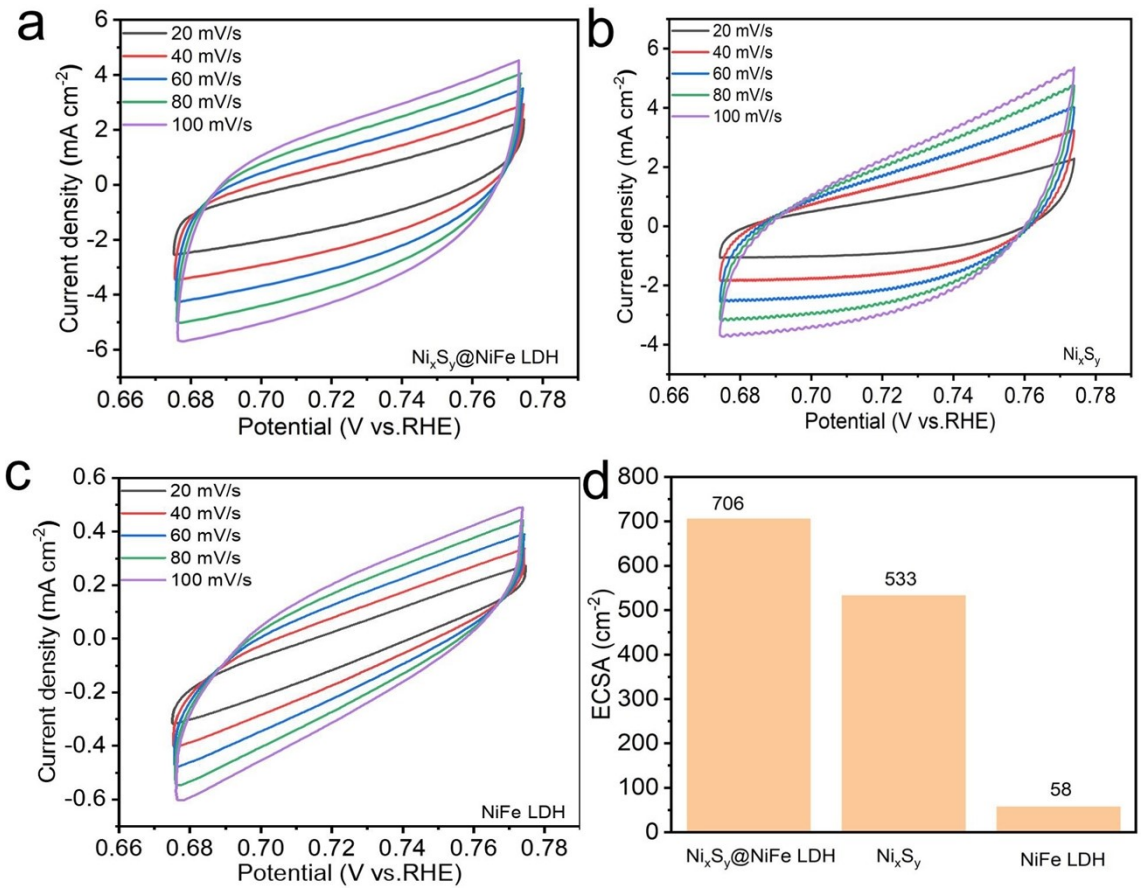

Figure S14. Cyclic voltammetry curves of (a) Ni_xS_y@NiFe LDH, (b) Ni_xS_y, (c) NiFe LDH in the region of 0.67-0.77 V vs. RHE. (d) The ECSA values of the fabricated samples.

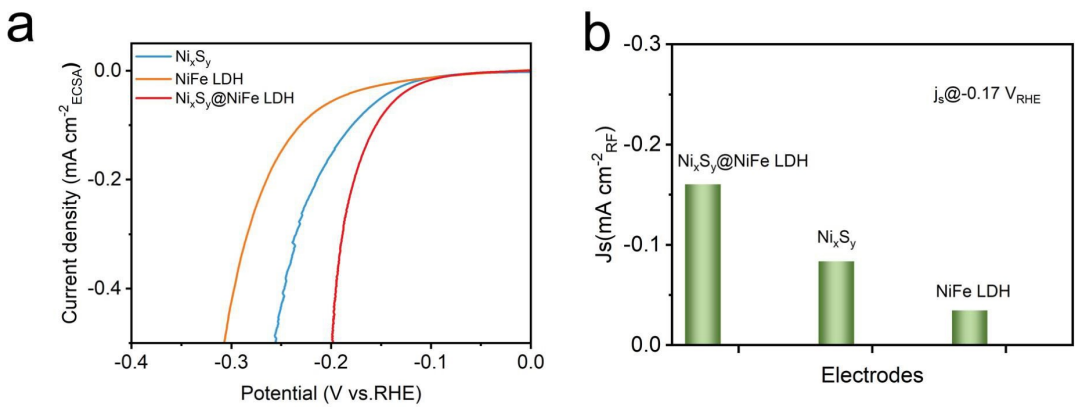

Figure S15. (a) ECSA normalized HER current densities (j_{ECSA}) of the electrodes. (b) The specific activity of the as-prepared electrodes in 1 M KOH solution at -0.17 V_{RHE}.

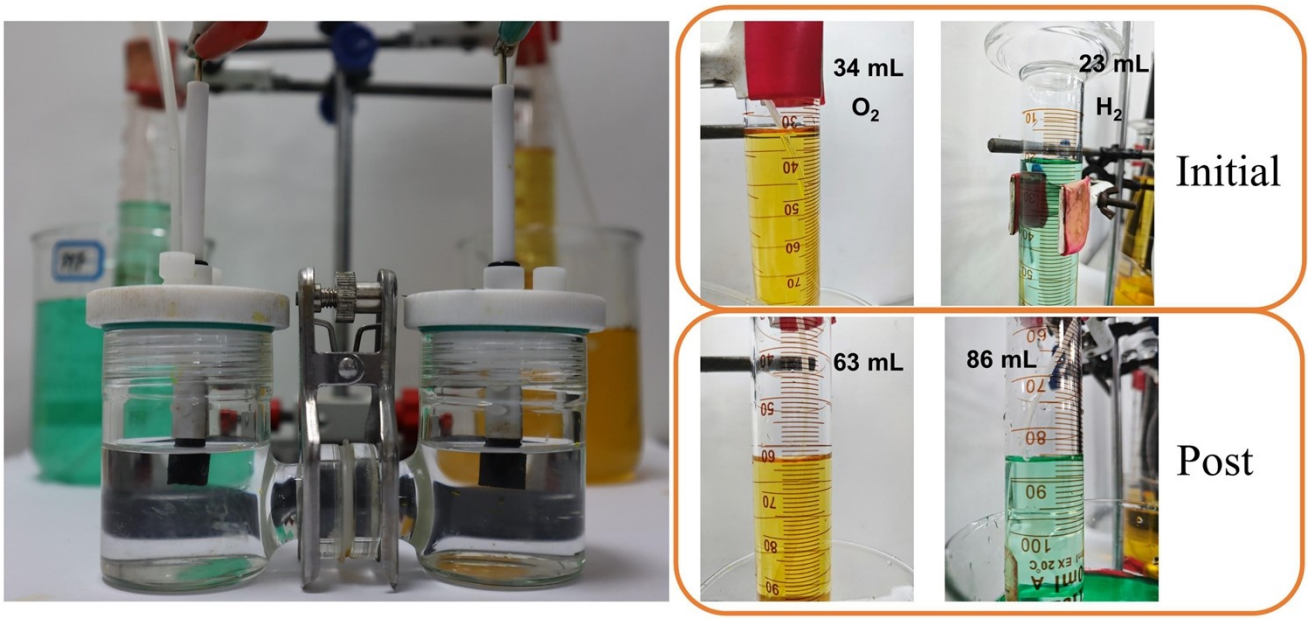

Figure S16. Ni_xS_y@NiFe LDH||Ni_xS_y@NiFe LDH double-electrodes system for overall water splitting and gas collection.

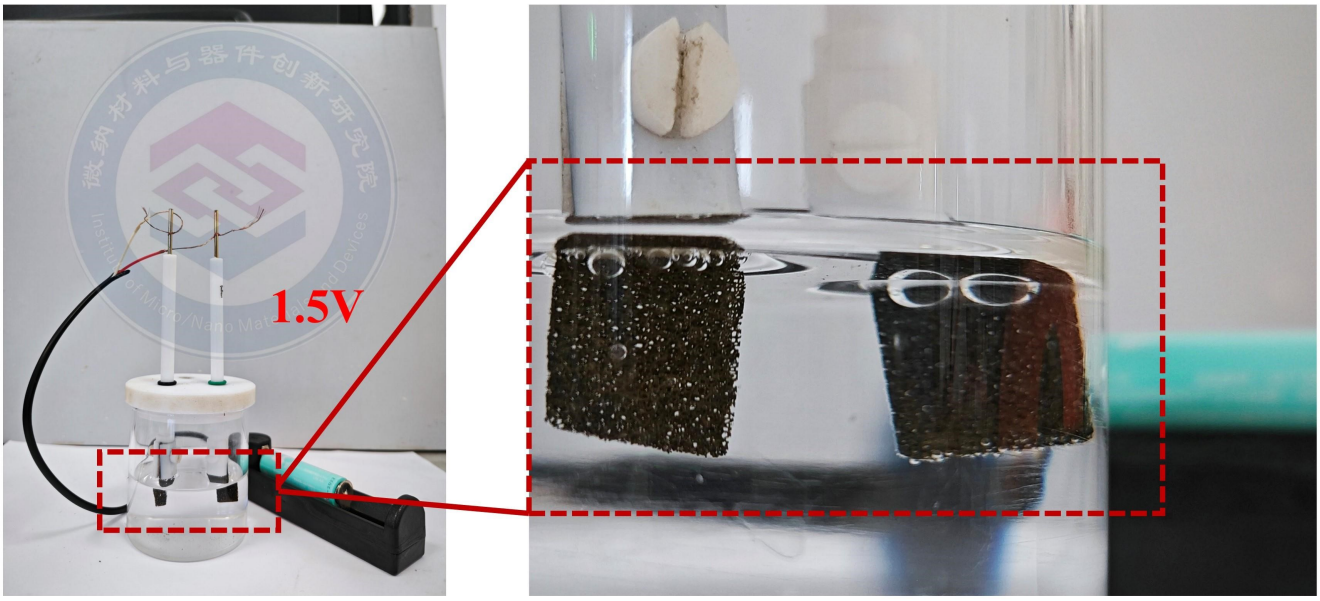

Figure S17. Optical images of Ni_xS_y@NiFe LDH||Ni_xS_y@NiFe LDH electrode driven by 1.5V battery at 1.0 M KOH.

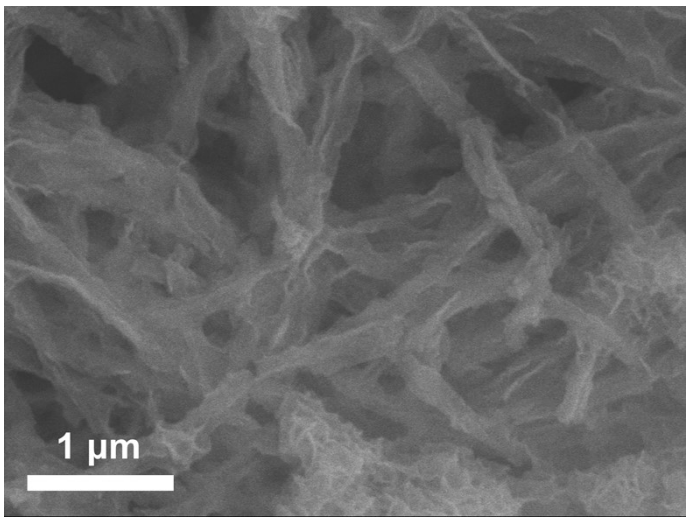

Figure S18. SEM images of Ni_xS_y@NiFe LDH after long-term stability test at 200 mA cm^{-2}.

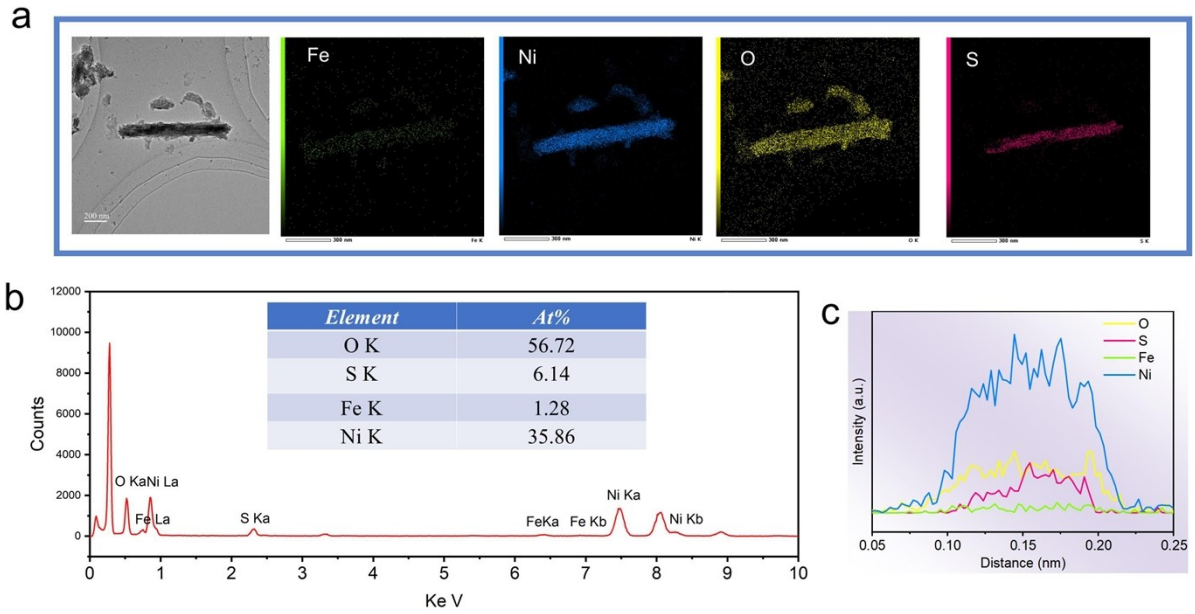

Figure S19. (a) STEM image and the corresponding elemental mapping images of Ni_xS_y@NiFe LDH, (b) EDS spectra of Ni_xS_y@NiFe LDH after OER stability test, (c) Line scan results of Fe, S, Ni and O elements in Ni_xS_y@NiFe LDH sample after OER stability test.

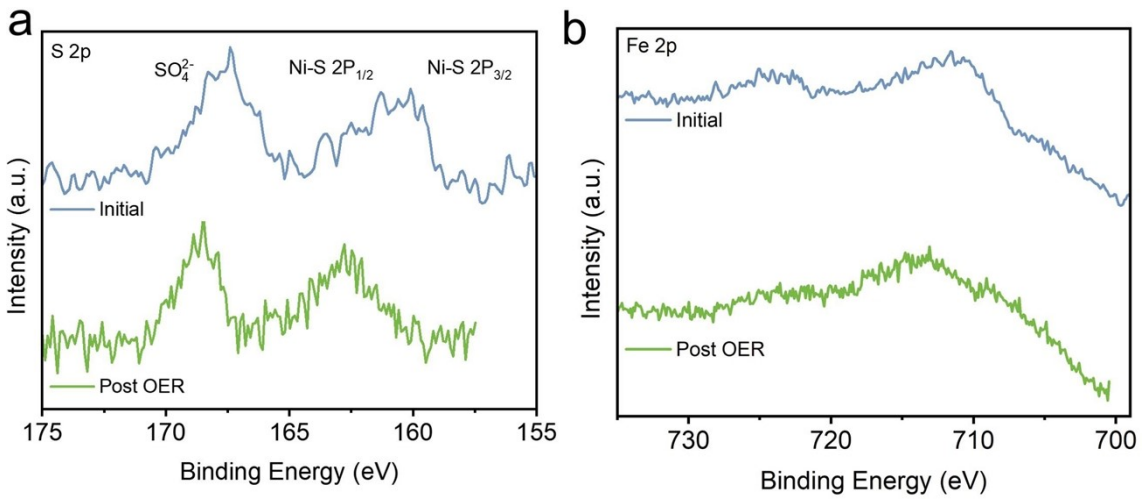

Figure S20. High-resolution XPS spectra of (a) S 2p and (b) Fe 2p for Ni_xS_y@NiFe LDH after OER test.

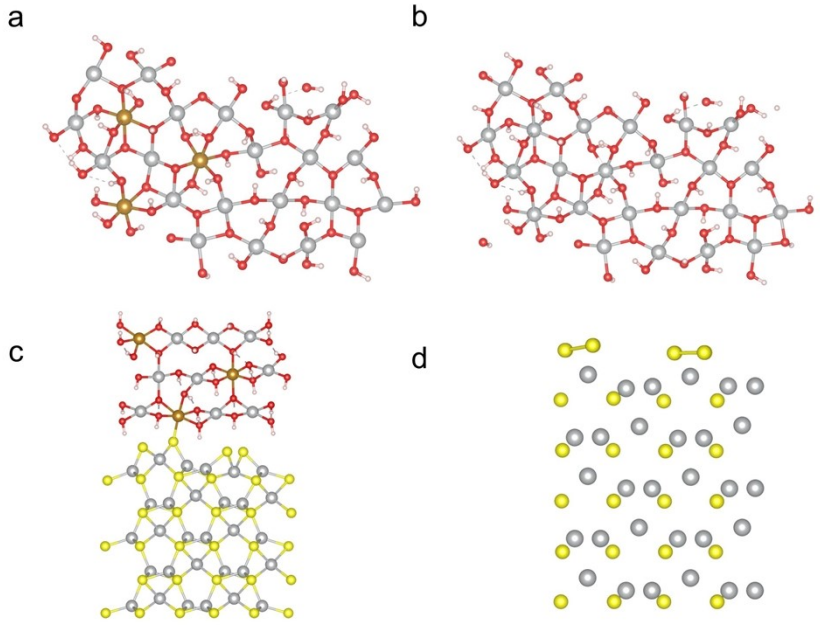

Figure S21. Structure models. (a) NiOOH@NiFeOOH; (b) NiOOH, (c) Ni_3S_2@NiFeOOH, (d) Ni_3S_2.

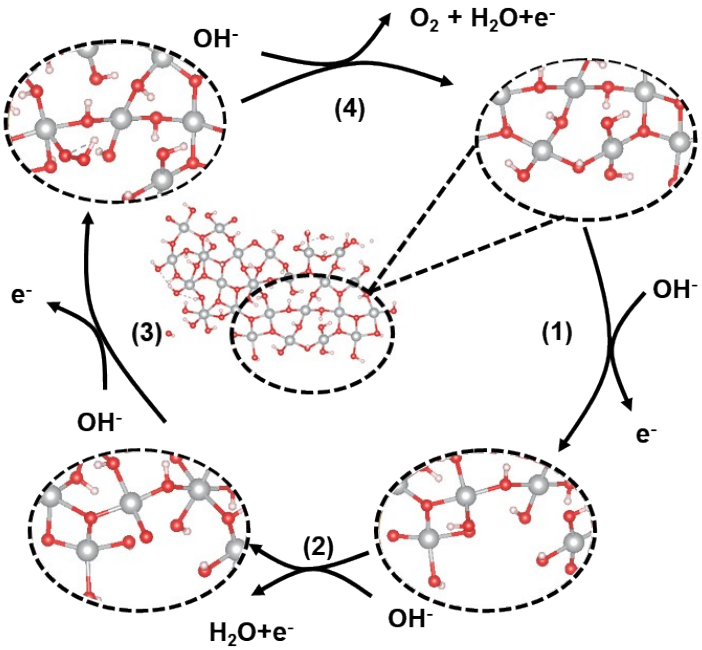

Figure S22. Structure model and schematic illustration of the HER pathway of NiOOH.

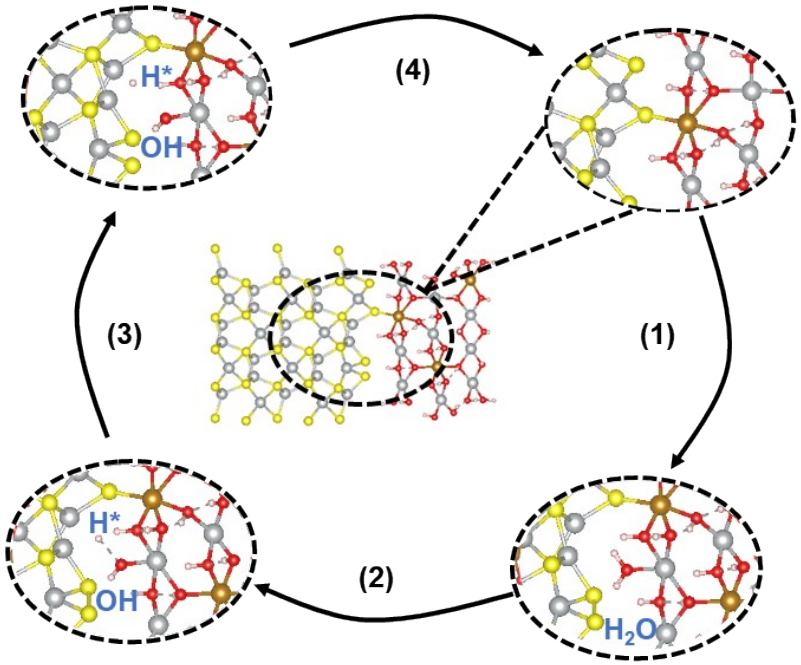

Figure S23. Structure model and schematic illustration of the HER pathway of Ni_xS_y@Ni^*Fe LDH.

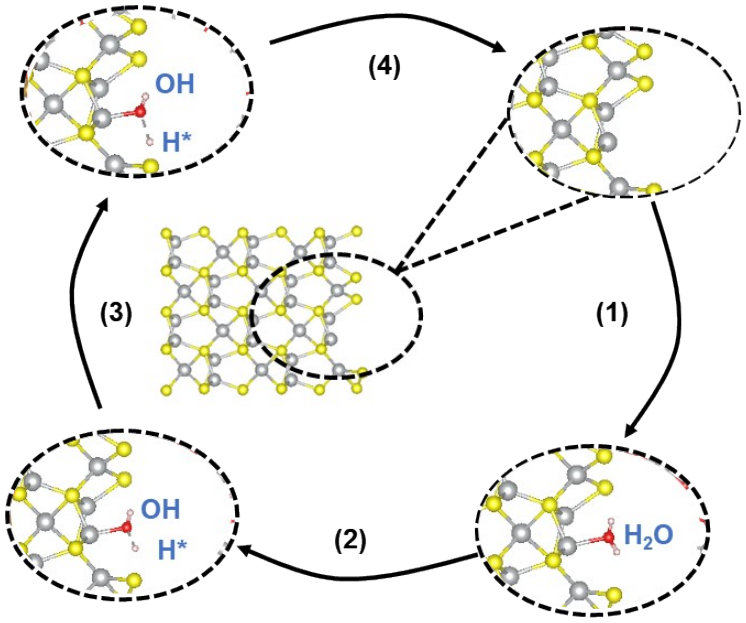

Figure S24. Structure model and schematic illustration of the HER pathway of $Ni_x{}^*S_y$.

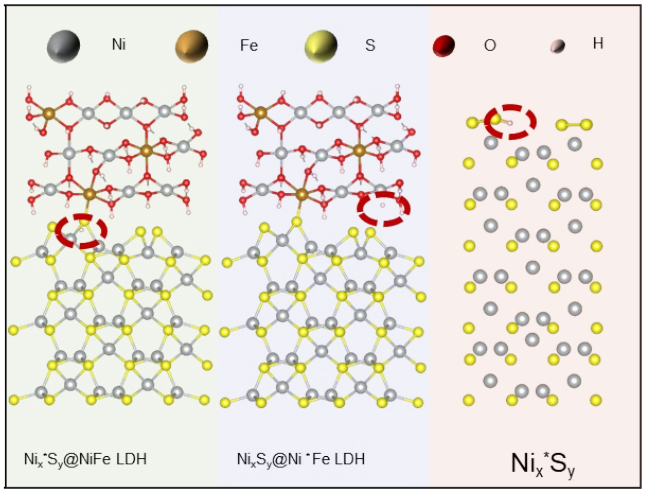

Figure S25. Structure model of $Ni_x{}^*S_y$@NiFe LDH, Ni_xS_y@Ni^*Fe LDH and $Ni_x{}^*S_y$.

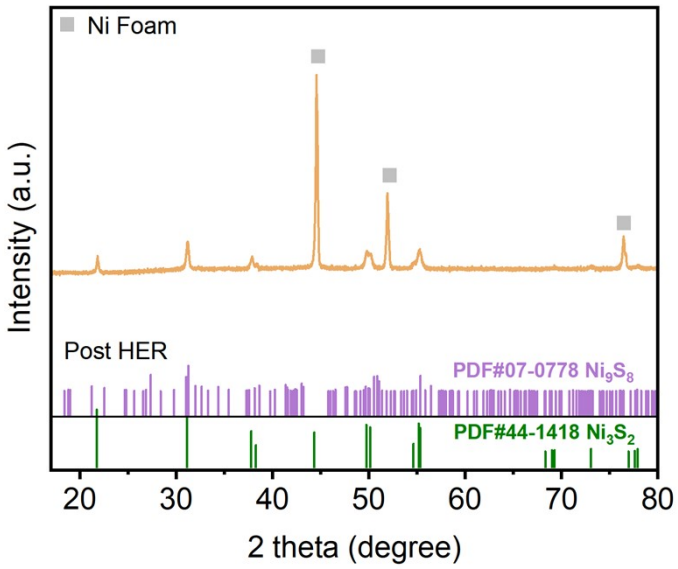

Figure S26. (a-b) XRD spectra of Ni_xS_y@NiFe LDH after HER test.

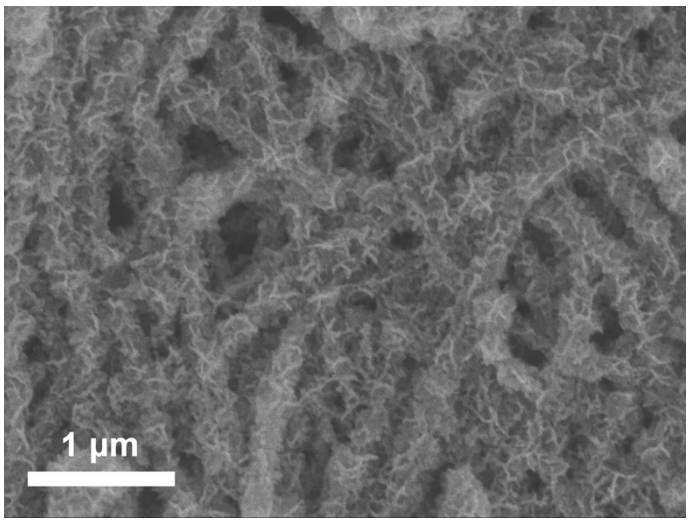

Figure S27. SEM images of Ni_xS_y@NiFe LDH after long-term stability test at -200 mA cm^{-2}.

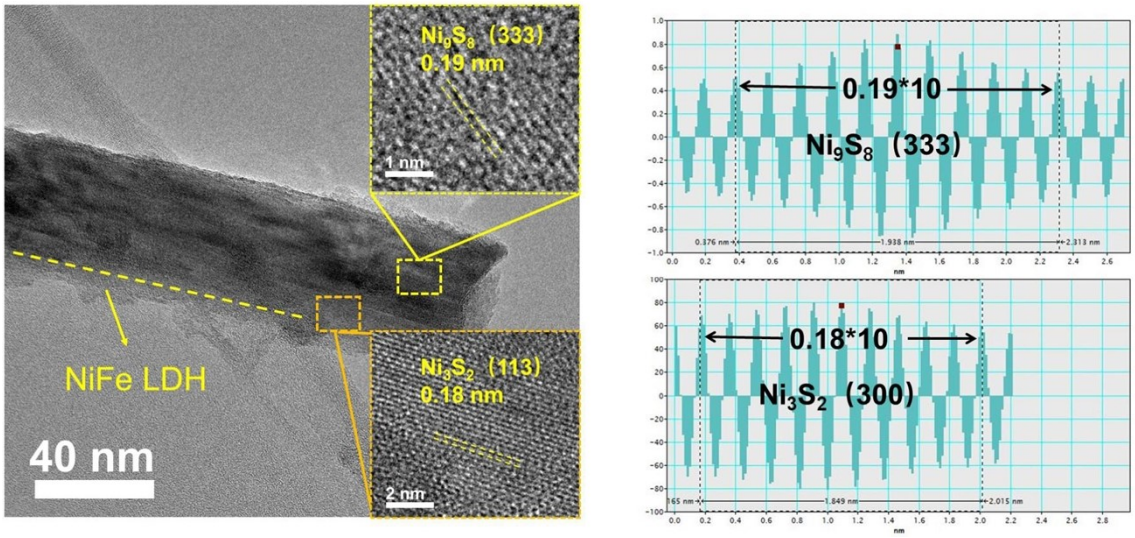

Figure S28. HRTEM images of Ni_xS_y@NiFe LDH after long-term stability test at -200 mA cm^{-2}

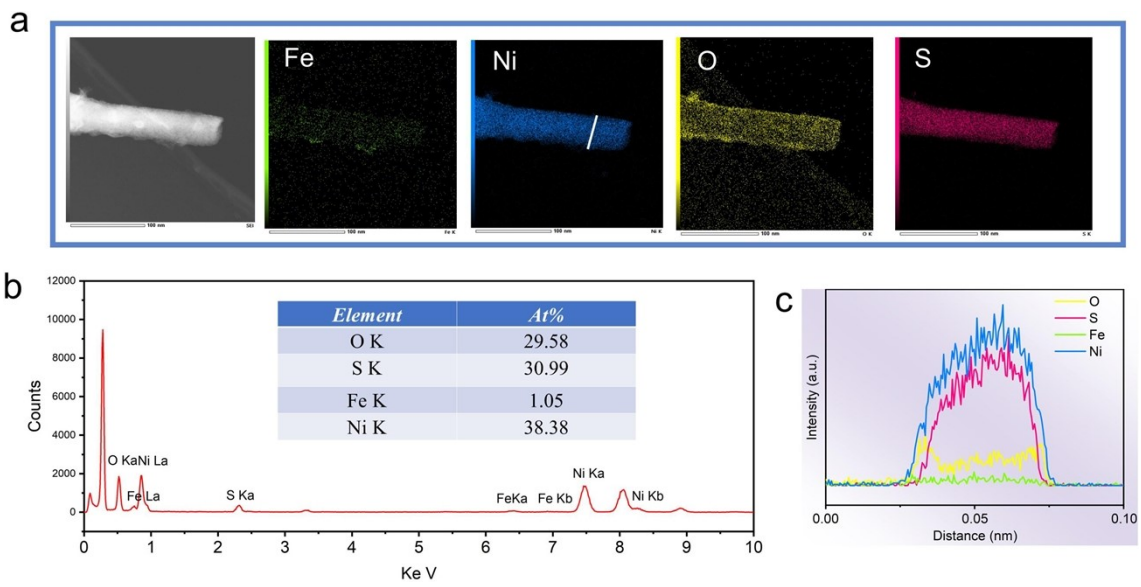

Figure S29. (a) STEM image and the corresponding elemental mapping images of Ni_xS_y@NiFe LDH, (b) EDS spectra of Ni_xS_y@NiFe LDH after HER stability test, (c) Line scan results of Fe, S, Ni and O elements in Ni_xS_y@NiFe LDH sample after OER stability test.

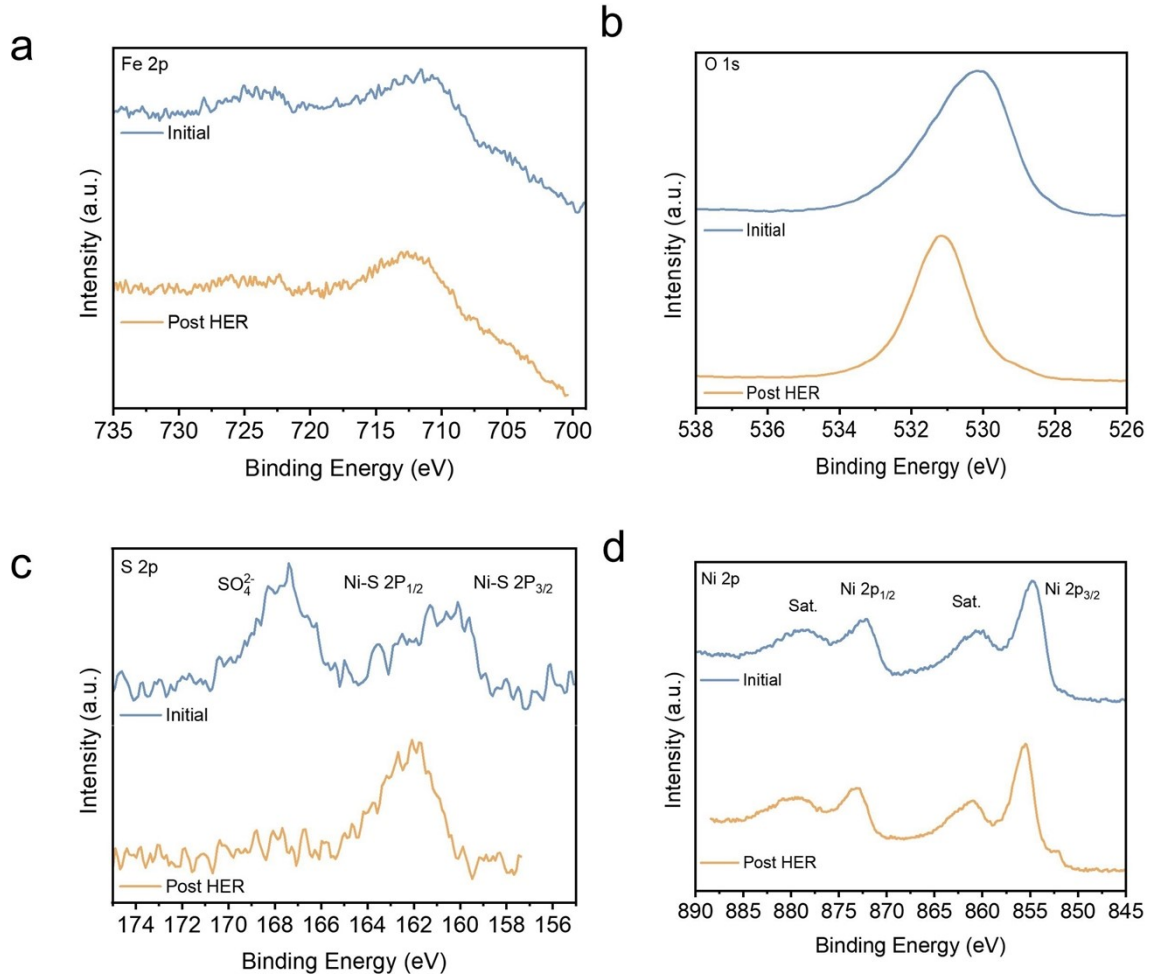

Figure S30. High-resolution XPS spectra of (a) Fe 2p, (b) O1s, (c) S2p, (d) Ni 2p in Ni_xS_y@NiFe LDH after HER test.

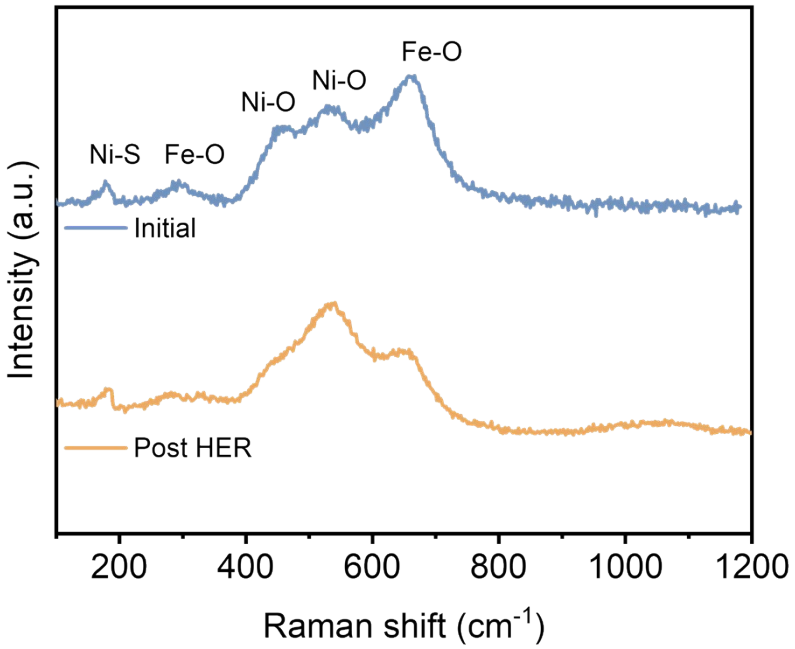

Figure S31. Raman spectra of Ni_xS_y@NiFe LDH after HER stability test for 250 h.

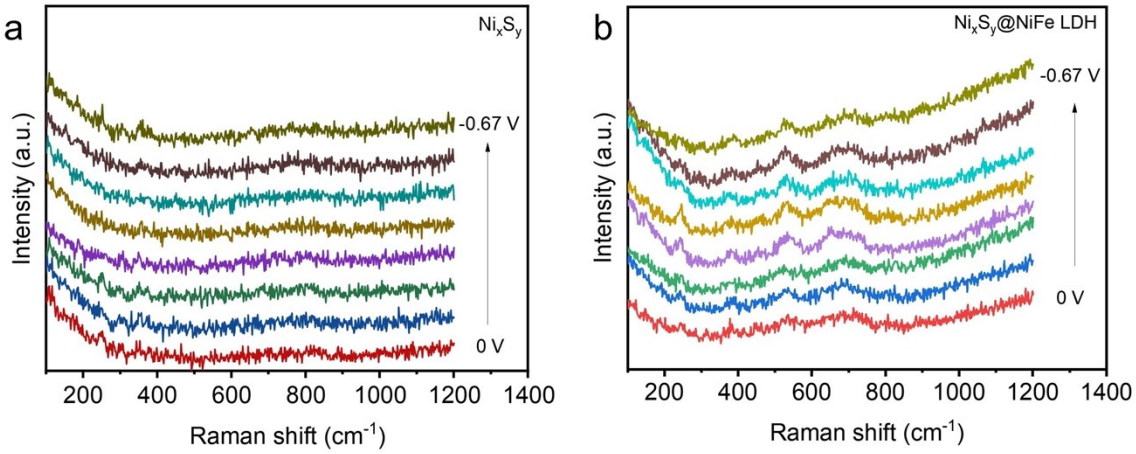

Figure S32. In-situ Raman spectra of (a) Ni_xS_y and (b) Ni_xS_y/NiFe LDH for HER.

Table S1. Weight percentage of Ni_xS_y@NiFe LDH, Ni_xS_y and NiFe LDH electrocatalyst were evaluated from ICP-OES results.

Samples	Fe (wt%)	Ni (wt%)
Ni_xS_y@NiFe LDH	3.5%	67.3%
Ni_xS_y	-	68.7%
NiFe LDH	3.3%	65.9%

Table.S2 Comparison of the OER performance of Ni_xS_y@NiFe LDH with other reported catalysts in 1.0 M KOH

Catalysts	J ($mA\ cm^{-2}$)	η (mV)	Tafel slope ($mV\ dec^{-1}$)	Stability	Ref.
Ni_xS_y@NiFe LDH	200	250	39.1	250 h@200 cm^{-2}	This work
	300	262			
$FeOOH/Ni_3S_2$	100	268	73	200 h@200 cm^{-2}	2
Ni_3S_2/NiFe LDH	50	230	25.6	250 h@100 cm^{-2}	3
Ni_3S_2-1.4%Fe	100	240	45	24 h@100 cm^{-2}	4
FeNiOOH	10	252	36.8	50 h@10 cm^{-2}	5
NiFe-OH/Ni_3S_2	100	256	62.6	120 h@100 cm^{-2}	6
Ni_3S_2/Ni_9S_8	40	280	38.8	24 h@10 cm^{-2}	7
Ni_2Fe_8-Ni_3S_2	100	235	55.28	300 h@1000 cm^{-2}	8
Zn-(Ni/FeOOH)@NF	100	269	72.7	1000 h@1000 cm^{-2}	9
$NiCo_2S_4$@NiFe LDH/NF	60	201	46.3	10 h@10 cm^{-2}	10
Ni_2Fe-LDH/$FeNi_2S_4$/NF	100	240	29.4	12 h@50 cm^{-2}	11
Ta-NiFe-LDH	100	280	59	20 h@100 cm^{-2}	12
NiFe-LDH/CNT	20	310	31	620 h@20 cm^{-2}	13

Table S3. EIS simulation according to the equivalent circuit inset in Fig. 3e.

Catalyst	R_s/Ω	CPE_1/mF		R_1/Ω	CPE_2/mF		R_{ct}/Ω
		CPE_T	CPE_P		CPE_T	CPE_P	
Ni_xS_y@NiFe LDH	1.221	3.084	0.76	0.11	4.83	0.91	0.91
Ni_xS_y	1.31	0.26	0.43	2.21	0.16	0.85	2.89
NiFe LDH	1.53	0.08	0.86	0.096	0.37	0.83	1.22
RuO_2-NF	1.35	0.44	0.75	12.68	0.21	12.76	12.76

Note: The Nyquist plots were fitted by a two-R-CPE circuit as shown by the model above the table. Each R-CPE unit consists of a resistance and a constant phase element (CPE_1 or CPE_2) in parallel, and CPE_T and CPE_p are related to interface uniformity and quality. where R_1 is related to the physical response of the porous structure of the electrode, R_{ct} and R_s represents the charge transfer resistance (R_{ct}) and electrolyte resistance (R_s) in the electrocatalytic HER and OER, respectively.

Table.S4 Comparison of the HER performance of Ni_xS_y@NiFe LDH with other reported catalysts in 1.0 M KOH.

Catalysts	J (mA cm^{-2})	η (mV)	Tafel slope (mV dec^{-1})	Stability	Ref.
	10	82			
Ni_xS_y@NiFe LDH	50	142	84.5	250 h@-200 cm^{-2}	This work
	100	159			
Ni_3S_2/NiFe LDH	10	61.3	72	200 h@-100 cm^{-2}	[3]
(Fe-Ni)Cox-OH/Ni_3S_2	100	254	98	110 h@-200cm^{-2}	[14]
P-$NiFeO_xH_y$	10	20.8	98	35 h@-100 cm^{-2}	[15]
$Ni(OH)_x/Ni_3S_2$	10	54	59	1000 h@-320 cm^{-2}	[16]
CoMoS/NiFeOOH	10	89	114	25 h@-50 cm^{-2}	[17]
N-Co_9S_8/Ni_3S_2/NF	10	111	88.6	20 h@-20 cm^{-2}	[18]
FQD/CoNi-LDH	10	150	181	20 h@-10 cm^{-2}	[19]
Ni_3S_2/NiCo LDH	10	156	145	12 h@-100 cm^{-2}	[20]
Ni_3S_2/VG@NiCo LDHs	10	120	87	24 h@-10 cm^{-2}	[21]
$NiCo_2S_4$@NiFe LDH/NF	10	200	101.1	24 h@-10 cm^{-2}	[10]
CuS/NiFe-LDH/NF	10	55	33	——	[22]
NiFe-LDH@CoS_x	10	200	62	24 h@-20 cm^{-2}	[23]
V-Ni_3S_2@NiFe LDH	10	120	104.4	24 h@-100 cm^{-2}	[24]
Ni1Fe10-LDH@Ni_3S_2/NF	20	197	99	12 h@-10 cm^{-2}	[25]

Table S5. EIS simulation according to the equivalent circuit inset in Fig. 4e.

Catalysts	R_s/Ω	CPE_1/mF		R_1/Ω	CPE_2/mF		R_{ct}/Ω
		CPE_T	CPE_P		CPE_T	CPE_P	
Ni_xS_y@NiFe LDH	1.31	0.11	0.48	0.11	0.11	0.78	5.23
Ni_xS_y	1.37	0.05	0.48	0.131	0.05	0.83	8.64
NiFe LDH	1.4	0.001	0.79	18.6	0.04	0.94	15.63
Pt/C-NF	1.19	0.006	0.78	0.37	0.73	0.74	0.81

Note: The Nyquist plots were fitted by a two-R-CPE circuit as shown by the model above the table. Each R-CPE unit consists of a resistance and a constant phase element (CPE_1 or CPE_2) in parallel, and CPE_T and CPE_p are related to interface uniformity and quality. where R_1 is related to the physical response of the porous structure of the electrode, R_{ct} and R_s represents the charge transfer resistance (R_{ct}) and electrolyte resistance (R_s) in the electrocatalytic HER and OER, respectively.

Table S6. Comparison of the overall water splitting performance of Ni_xS_y@NiFe LDH with other reported catalysts in 1.0 M KOH

Catalysts	J (mA cm^{-2})	η (V)	Stability	References
Ni_xS_y@NiFe LDH	10	1.48	120 h@50 cm^{-2}	This work
	50	1.66		
NiOOH/FeOOH NBs||NiFeP NBs	10	1.53	400 h@100 cm^{-2}	[26]
Ni_3S_2@Ni_9S_8	10	1.62	24 h@20 cm^{-2}	[27]
N-Ni_3S_2@C	10	1.57	140 h@100 cm^{-2}	[28]
NiFeLDH/CC||Co-NMS/CA	10	1.66	10 h@10 cm^{-2}	[29]
Ni_3S_2/VG@NiCo LDHs	10	1.56	24 h@20 cm^{-2}	[21]
$NiCo_2S_4$@NiFe LDH	10	1.6	12 h@10 cm^{-2}	[10]
NiFe-LDH@CoS_x/NF	10	1.537	24 h@20 cm^{-2}	[23]
Ni1Fe10-LDH@Ni_3S_2/NF	10	1.65	12 h@10 cm^{-2}	[25]

Reference

1. P. Thangavel, H. Lee, T. H. Kong, S. Kwon, A. Tayyebi, J. h. Lee, S. M. Choi and Y. Kwon, *Adv. Energy Mater.*, 2023, **13**, 2203401.
2. M. Chen, Y. Zhang, J. Chen, R. Wang, B. Zhang, B. Song and P. Xu, *Small*, 2024, **20**, 2309371.
3. S.-W. Wu, S.-Q. Liu, X.-H. Tan, W.-Y. Zhang, K. Cadien and Z. Li, *Chem. Eng. J.*, 2022, **442**, 136105.
4. L. Zhang, Q. Xu, R. Zhao, Y. Hu, H. Jiang and C. Li, *Green Chem. Eng.*, 2022, **3**, 367-373.
5. Z. Wang, Q. Lei, Z. Wang, H. Yuan, L. Cao, N. Qin, Z. Lu, J. Xiao and J. Liu, *Chem. Eng. J.*, 2020, **395**, 125180.
6. J. Zhang, H. Yu, J. Yang, X. Zhu, M. Hu and J. Yang, *J. Alloys Compd.*, 2022, **924**, 166613.
7. Y. Deng, W. Lai, L. Ge, H. Yang, J. Bao, B. Ouyang and H. Li, *Inorg. Chem.*, 2023, **62**, 3976-3985.
8. G. Ding, H. Lee, Z. Li, J. Du, L. Wang, D. Chen and L. Sun, *Adv. Energy Sustainability Res.*, 2022, **4**, 2200130.
9. X. Zhang, H. Yi, M. Jin, Q. Lian, Y. Huang, Z. Ai, R. Huang, Z. Zuo, C. Tang, A. Amini, F. Jia, S. Song and C. Cheng, *Small*, 2022, **18**, 2203710.
10. J. Liu, J. Wang, B. Zhang, Y. Ruan, L. Lv, X. Ji, K. Xu, L. Miao and J. Jiang, *ACS Appl. Mater. Interfaces*, 2017, **9**, 15364-15372.
11. L. Tan, J. Yu, C. Wang, H. Wang, X. Liu, H. Gao, L. Xin, D. Liu, W. Hou and T. Zhan, *Adv. Funct. Mater.*, 2022, **32**, 2200951.
12. X. Wang, Y. Tuo, Y. Zhou, D. Wang, S. Wang and J. Zhang, *Chem. Eng. J.*, 2021, **403**, 126297.
13. M. Gong, Y. Li, H. Wang, Y. Liang, J. Z. Wu, J. Zhou, J. Wang, T. Regier, F. Wei and H. Dai, *J. Am. Chem. Soc.*, 2013, **135**, 8452-8455.
14. Q. Che, Q. Li, X. Chen, Y. Tan and X. Xu, *Appl. Catal. B*, 2020, **263**, 118338.
15. Q. Li, Q. Chen, S. Lei, M. Zhai, G. Lv, M. Cheng, L. Xu, H. Xu, Y. Deng and J. Bao, *J. Colloid Interface Sci.*, 2023, **631**, 56-65.
16. W. He, R. Zhang, D. Cao, Y. Li, J. Zhang, Q. Hao, H. Liu, J. Zhao and H. L. Xin, *small*, 2023, **19**, 2205719.
17. W. Mai, Q. Cui, Z. Zhang, D. Wen, L. Tian and W. Hu, *Int. J. Hydrogen Energy*, 2021, **46**, 24078-24093.
18. H. Xie, Y. Feng, X. He, Y. Zhu, Z. Li, H. Liu, S. Zeng, Q. Qian and G. Zhang, *Small*, 2023, **19**, 2207425.
19. Y. Feng, X. Wang, J. Huang, P. Dong, J. Ji, J. Li, L. Cao, L. Feng, P. Jin and C. Wang, *Chem. Eng. J.*, 2020, **390**, 124525.
20. L. Jia, G. Du, D. Han, Y. Hao, W. Zhao, Y. Fan, Q. Su, S. Ding and B. Xu, *J. Mater. Chem. A*, 2021, **9**, 27639-27650.
21. X. Zhang, J. Fan, X. Lu, Z. Han, C. Cazorla, L. Hu, T. Wu and D. Chu, *Chem. Eng. J.*, 2021, **415**, 129048.
22. B. Sarfraz, I. Bashir and A. Rauf, *Fuel*, 2023, **337**, 127253.
23. Y. Yang, Y. Xie, Z. Yu, S. Guo, M. Yuan, H. Yao, Z. Liang, Y. R. Lu, T.-S. Chan, C. Li, H. Dong and S. Ma, *Chem. Eng. J.*, 2021, **419**, 129512.
24. J. Zhou, L. Yu, Q. Zhu, C. Huang and Y. Yu, *J. Mater. Chem. A*, 2019, **7**, 18118-18125.
25. L. Ren, C. Wang, W. Li, R. Dong, H. Sun, N. Liu and B. Geng, *Electrochim. Acta*, 2019, **318**, 42-50.
26. P. Yan, Q. Liu, H. Zhang, L. Qiu, H. B. Wu and X.-Y. Yu, *J. Mater. Chem. A*, 2021, **9**, 15586-15594.
27. G. Zhao, Y. Xing, Y. Liu, X. Wang, B. Zhang, L. Mu, W. Liao and X. Xu, *Mater. Today Chem.*, 2023, **34**, 101758.
28. Q. Hao, S. Li, H. Liu, J. Mao, Y. Li, C. Liu, J. Zhang and C. Tang, *Catal. Sci. Technol.*, 2019, **9**, 3099-3108.

29. L. Zhang, Y. Zheng, J. Wang, Y. Geng, B. Zhang, J. He, J. Xue, T. Frauenheim and M. Li, *Small*, 2021, **17**, 2006730.